REPORT DOCUMENTATION PAGE

Form Approved
OMB No. 0704-0188

1. REPORT DATE *(DD-MM-YYYY)*	2. REPORT TYPE	3. DATES COVERED *(From - To)*
June 23, 2008	Final report	

4. TITLE AND SUBTITLE

Biologically Inspired Artificial Haircell Sensors

5a. CONTRACT NUMBER

5b. GRANT NUMBER
FA9550-05-1-0041

5c. PROGRAM ELEMENT NUMBER

6. AUTHOR(S)
Chang Liu

5d. PROJECT NUMBER

5e. TASK NUMBER

5f. WORK UNIT NUMBER

7. PERFORMING ORGANIZATION NAME(S) AND ADDRESS(ES)

University of Illinois at
Urbana-Champaign
Urbana, IL 60801

8. PERFORMING ORGANIZATION REPORT NUMBER

9. SPONSORING / MONITORING AGENCY NAME(S) AND ADDRESS(ES)

Jennifer Gresham, AFOSR
875 N. Randolph Street, Suite 325, Room 3112
Arlington, VA

10. SPONSOR/MONITOR'S ACRONYM(S)

11. SPONSOR/MONITOR'S REPORT NUMBER(S)

12. DISTRIBUTION / AVAILABILITY STATEMENT

Dist A

13. SUPPLEMENTARY NOTES

14. ABSTRACT

The use and development of unmanned aircraft has significantly increased recently. As electronics packages and equipment have decreased in size and weight, so have the potential dimensions of these aircraft. The ability of these vehicles to retain acceptable lift is highly sensitive to separation of flow over the lift surface

The team developed the design and fabrication process for high sensitivity artificial haircell sensors and characterized their performances. The sensors were able to measure air flow rate with a detection limit of 10 mm/s. The team performed simultaneous sensor reading and micro PIV (particle imaging velocimetry) tests. The sensors were mounted on scaled models of airfoils. Belinda Batten's group built numerical model of the hair and extracted higher order models. The team also developed custom morphing wing micro air vehicle.

The project successfully established haircell flow sensors, developed reduced control model for such sensors, and characterized the flow field using both haircell sensors and particle imaging velocimetry (PIV) methods.

15. SUBJECT TERMS

Flow sensors, flow separation, micro air vehicle, reduced order model

16. SECURITY CLASSIFICATION OF:			17. LIMITATION OF ABSTRACT	18. NUMBER OF PAGES	19a. NAME OF RESPONSIBLE PERSON
a. REPORT	b. ABSTRACT	c. THIS PAGE			19b. TELEPHONE NUMBER *(include area code)*

OBJECTIVES

Micro air vehicles, especially morphing wing MAVs, are of importance for air force and military applications. The stability and agility of such vehicles play critical role in defining the functionality and range of use. This project is aimed at developing artificial haircell flow sensors following biological inspiration of insect flow sensors, and demonstrate the potentials of these sensors for controlling the flight of micro air vehicles (MAV). A second objective is to investigate the fluid dynamic characteristics of the sensor-wing assembly. A third objective is to develop reduced order numerical models of the sensors for control purposes.

STATUS OF EFFORTS

The team developed the design and fabrication process for high sensitivity artificial haircell sensors and characterized their performances. The sensors were able to measure air flow rate with a detection limit of 10 mm/s. The team performed simultaneous sensor reading and micro PIV (particle imaging velocimetry) tests. The sensors were mounted on scaled models of airfoils. Belinda Batten's group built numerical model of the hair and extracted higher order models. The team also developed custom morphing wing micro air vehicle.

The project successfully established haircell flow sensors, developed reduced control model for such sensors, and characterized the flow field using both haircell sensors and particle imaging velocimetry (PIV) methods.

ACCOMPLISHMENTS

Background

The use and development of unmanned aircraft has significantly increased recently. As electronics packages and equipment have decreased in size and weight, so have the potential dimensions of these aircraft. Specifically, a classification of micro-air-vehicles (MAVs) has emerged which limits the scale of the aircraft to approximately 6 inches (15 cm). Typically these craft are operated at low Reynolds numbers ($Re<10^6$). The ability of these vehicles to retain acceptable lift is highly sensitive to separation of flow over the lift surface. McCullough and Gault [1] discussed the now generally accepted three main types of airfoil stall: trailing edge, leading edge and thin airfoil stall. Flow over a thin, flat airfoil at high angles of attack displays attributes of thin airfoil stall; the flow separates at the leading edge with a reattachment point which moves downstream as angle of attack increases. McCullough and Gault likened this to the separation of flow past a sharp edge because at higher angles of attack the stagnation point moves below the leading edge.In this present study, two types of flow events are of interest as depicted in Figure 1, the small scale disturbances associated with leading edge separation and the larger flow features which develop for completely separated flow at high angles of attack. The small scale structures formed at the leading edge are related to a Kelvin-Helmholtz instability between the freestream and recirculating flow which rolls up to form vortices. The larger structures formed in the wake of an airfoil in completely separated flow are more aligned with the von Kármán process for vortex shedding from bluff bodies. Increased knowledge of the flow events leading up to and during separation will be valuable to the development of unmanned airplanes and more specifically, autonomous aircraft. Moreover, detailed understanding of the time dependent nature of separation conditions may lead to the ability for new control algorithms to improve overall performance. Identifying the development and behavior of structures in low Reynolds number flow over an airfoil is of importance to flow control techniques. It has been observed that the production of these structures may be periodic or at least have some characteristic frequencies associated with the large vortical structures. Understanding this process may lead to improved techniques for delaying or counteracting separation effects under these conditions.

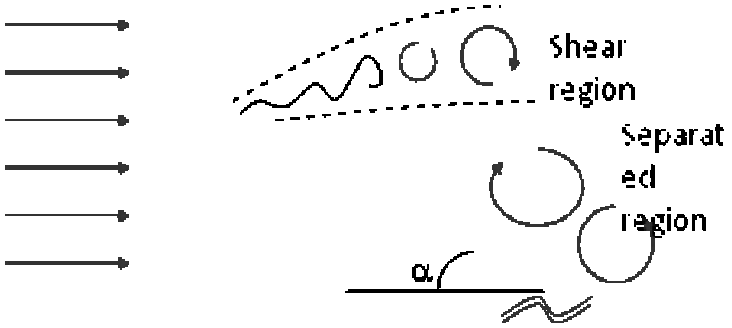

Figure 1: Flow separation on airfoil.

Separation of airflow over a wing has been a topic of interest for many decades. Studies of high Reynolds flows have direct application to traditional aircraft. In contrast, Carmichael [2] compiled a detailed survey of low Reynolds airfoil performance. This study identified various flow regimes based on Reynolds number as well as the process of separation and characteristics of the separation bubble which leads to a discussion on boundary layer trip devices. In the regime of Re = 10,000 to 30,000 he noted that small gliders operate in a completely laminar manner and that trip devices had little benefit. At larger Reynolds numbers, Re = 30,000 to 70,000, airfoils must be designed with higher aspect ratios due to induced drag. This regime received additional attention because it also coincides with aircraft operating in rarefied environments such as extremely high altitude or the Martian atmosphere.

More recently the investigation of low Reynolds number flows has increased as a result of interest in autonomous air vehicle development. In general these craft operate at Reynolds numbers less than or equal to 100,000. Mueller and DeLaurier [3] put forth a review of small air vehicles which includes the aerodynamics for fixed and flapping wing vehicles. Discussion of the Reynolds number effects on the separation bubble is included. At very low Reynolds numbers, less than 50,000, there is no reattachment of the flow for leading edge separation.Distinct differences in flight characteristics between high Reynolds number Re>500,000 and lowReynolds number craft necessitate a different design approach for emerging MAV's.

The effect of periodic flow can be significant on the body forces for low Reynolds regimes. Much work has been done to analyze the von Kármán process of vortex shedding from blunt bodies. Bishop and Hassan [4] and Berger and Wille [5] describe the phase synchronization of fluctuations for a cylinder in cross-flow and its wake at low Reynolds numbers. Mair and Maull [6] reviewed various findings including the three dimensional effects of vortex formation on the body forces. The strongest effect was seen when the vortices were large in the spanwise direction along the length of the cylinder. This effect was also seen for airfoils with blunt trailing edges. One solution from their review for the reduction of this effect was to introduce a serrated trailing edge, which produced streamwise vortices that disrupted the formation of longitudinal vortex structures.

Development of the sensors

Artificial haircell sensors were developed based on both polymer and silicon materials. Shown in Figure 2 is a scanning electron micrograph of a silicon haircell sensor [7], which consists of a silicon cantilever with a vertical hair at its distal end. The vertical hair is made of photodefinable epoxy material (SU-8). Fluid flow acting on the vertical hair introduces drag force to it and develops a bending torque on the cantilever. The torque in turn develops surface stress at the base of the cantilever.

Individual silicon sensors are then packaged to provide robustness and electrical access. The picture of a packaged sensor is shown in Figure 3. The cantilever beam is 200 μm long, 20 μm wide, and 2 μm thick. The hair is typically 100-750 μm tall. The height of the hair is controlled by the thickness of the deposited layer. The resonant frequency of the cantilever is approximately 1-5 kHz, depending on the dimensions of the cantilever and the hair.

A high-yield process for fabricating the sensors has been invented. The sensor is fabricated using a silicon-on-insulator wafer (SOI), with the top silicon layer's thickness being the thickness of the silicon cantilever. First,

the SOI wafer is selectively doped to form piezoressitors for strain sensing. Secondly, the wafer is photolithographically defined using photoresist and etched with plasma etching until the underlying silicon oxide insulator layer is exposed. The backside of the wafer is then patterned and etched using deep reactive ion etching method to define the backside cavity. A front side deposition of photodefinable epoxy is carried out, followed by photo exposure to define the hairs. However, development of photosensitive polymer is not performed immediately. The oxide is removed by backside etching. After this step, the wafer is diced into chips and then the photo definable epoxy is developed.

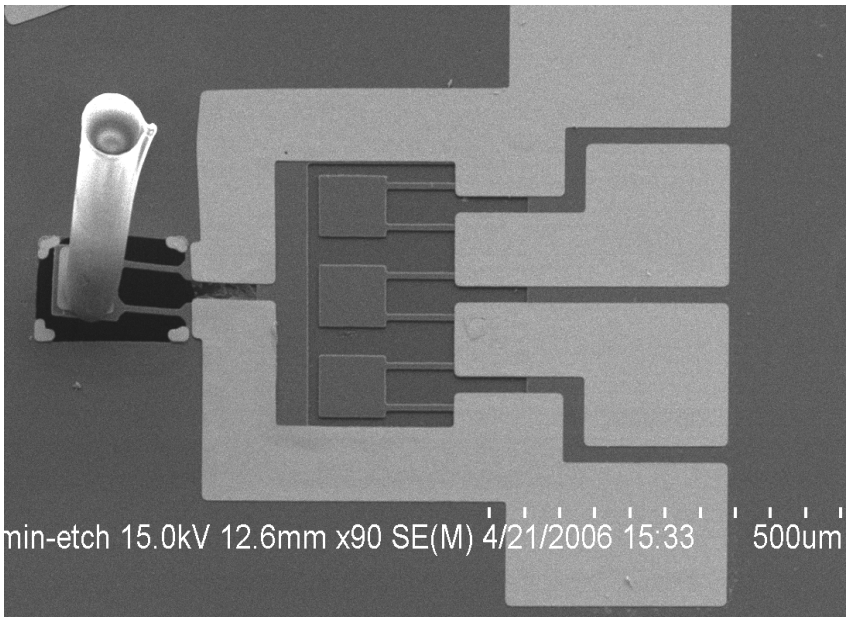

Figure 2: SEM micrograph of a single haircell sensor.

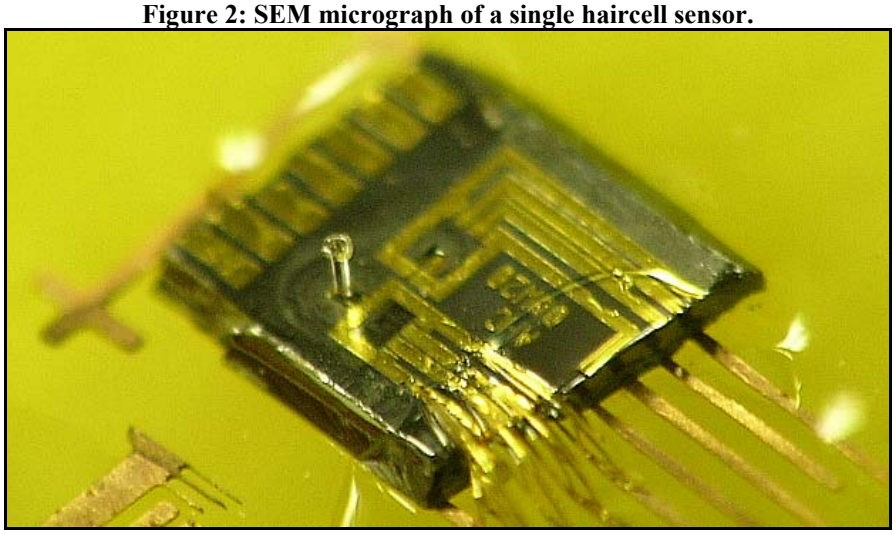

Figure 3: Photo of a packaged haircell sensor. Electrical leads are provided by wire bonding.

Sensor-wing assembly

Sensors are packaged and placed on aerodynamic airfoils with flush mounting. Towards this end, we first machine airfoil structures and then produce groves of controlled dimensions which match those of the haircell chip. The sensorized airfoil is then placed in a flow tunnel. A diagram of such arrangement is shown in Figure 4. Figure 5 shows pictures of airfoils in the wind tunnel and close-up view of mounted sensors.

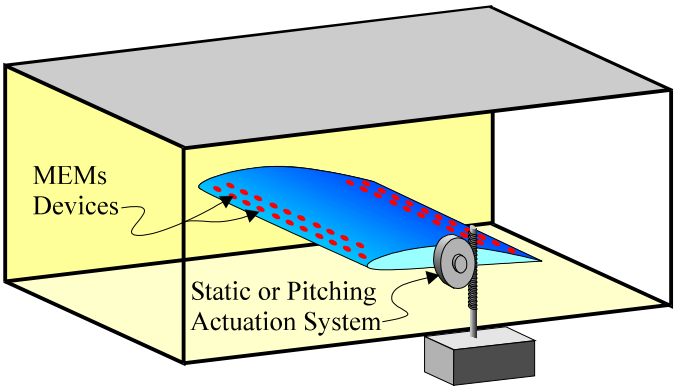

Figure 4: Concept drawing of sensor package on an airfoil, which in turn is placed inside a wind tunnel.

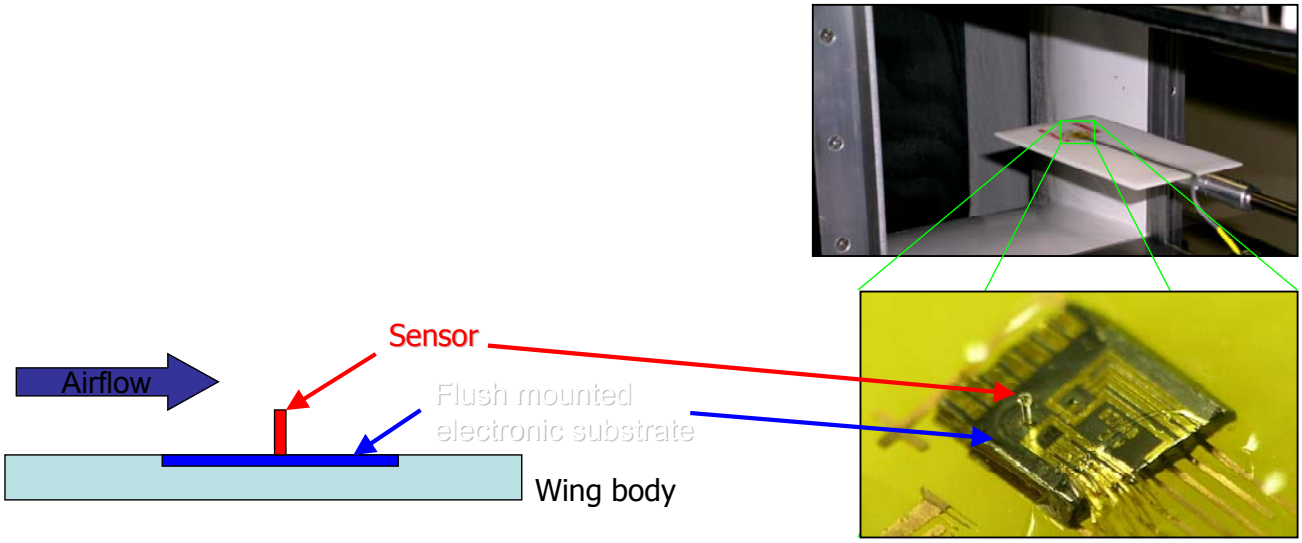

Figure 5: Photos of the air foil and the attached sensor.

The wing is attached to a six-degree-of-freedom balance that measures the moment and force applied to the wing. The measured lift as a function of the angel of attach in a typical configuration is illustrated in Figure 8.

Tests were carried out in a large recirculating wind tunnel with internal dimensions of 1.37x1.52 m (Figure 6, Figure 7). A Laskin nozzle was used to generate airborne particles in the tunnelusing vegetable oil. Particle size distribution was centered around 6 μm. This corresponds to a particle response time limit of 5 kHz using a Stokes flow drag model described by Hinze [8]. A 532 nm New Wave Pegasus Laser was used to illuminate the flow from the downstream direction. A Dantec Dynamics 9080x0651 light sheet module was used to convert the beam to a 1 mm wide light sheet. This light sheet was placed in the spanwise center of the airfoil.

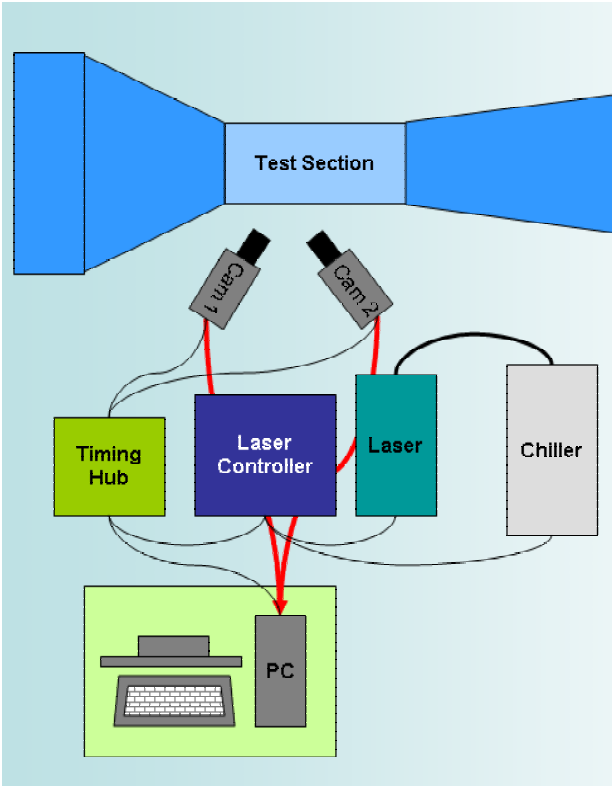

Figure 6: Schematic diagram of the wind tunnel setup.

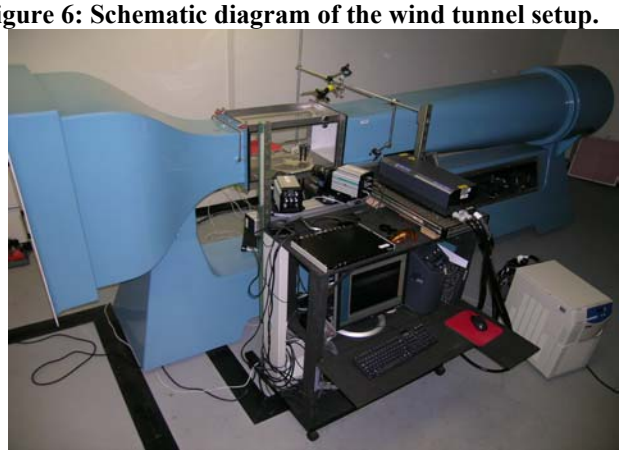

Figure 7: Photo of the wind tunnel setup.

The airfoil was a flat plate of aspect ratio 1:2 (span to chord) and chord length of 20.5 cm. The plate leading and trailing edges were elliptical with ratio of 5:1. The thickness of the airfoil was approximately 2% of the chord length, 4 mm. The airfoil was supported from the trailing edge.

Three freestream velocities were used for this study: 1.1, 2.0 and 5.0 m/s which correspond to chord Reynolds numbers of 14,700, 26,700 and 66,700. Four angles of attack were investigated at each velocity: 14°, 16°, 18° and 20°, for a total of 12 experimental cases. For each case images were obtained using an iNanosense high speed digital camera equipped with an image intensifier. The resolution of the CCD was 1280x1024 and the field of view was approximately 55x42 mm. Synchronization with the laser pulse was done using Dantec Dynamics FlowManager software. Time delay between laser pulses for these data was 50 μs for the Re = 66,700 cases and 100 μs for the Re = 14,700 and 26,700 cases. The time resolved sampling of velocity fields was performed at 500 Hz. The total sample time was 2.0 seconds due to hardware memory limitations. This resulted in a 0.25 Hz frequency resolution when determining the velocity spectra. It is understood this may not be appropriate for analysis of low frequency events but it provides adequate results for higher frequency rates greater than > 10 Hz. Even so, the low frequency results will be shown to match reasonably well with previously accepted results.

Post processing of the images was done to reduce glare from the airfoil surface. This was done by performing a pixel mean intensity calculation and removing the mean value from each image. The subregion size for each

PIV cross correlation calculation was 32x32 pixels with 50% overlap. This resulted in a vector field of 79x63 grid points with a spacing of approximately 0.6 mm. Erroneous or missing data from the velocity field were eliminated using a 3x3 median filter. This accounted for less than 1% of the data for the Re = 14,700 and 26,700 cases and less than 5% of the Re = 66,700 cases.

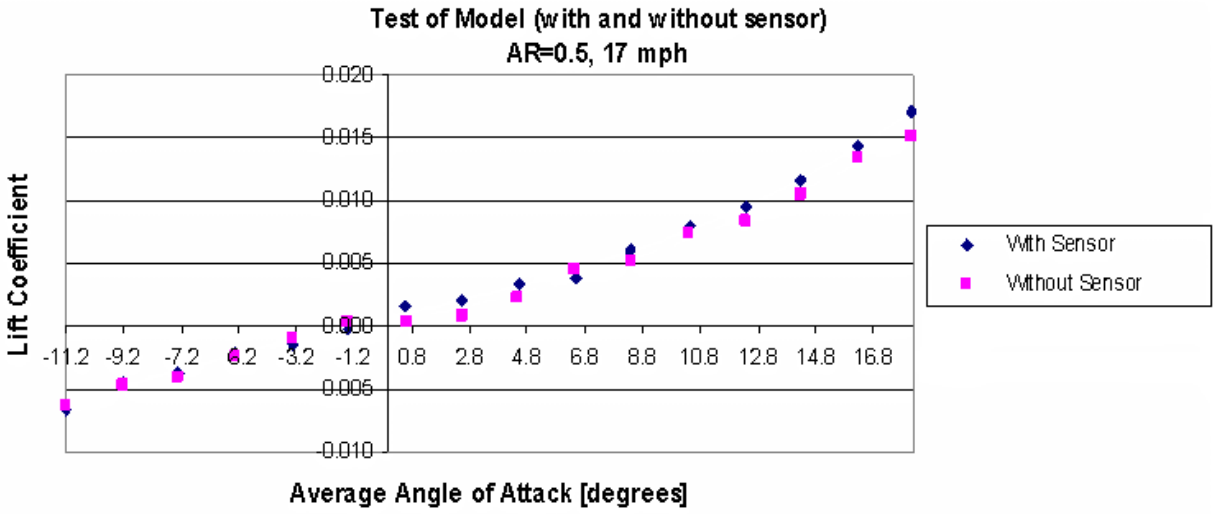

Figure 8: Measured lift coefficient vs. the angle of attack for the air foil, with and without the sensors mounted.

The output of the sensor is a function of the inflow velocity. A representative plot of the sensor response is shown in Figure 9. As shown, the output voltage is a parabolic function of the input velocity, as predicted by fluid models.

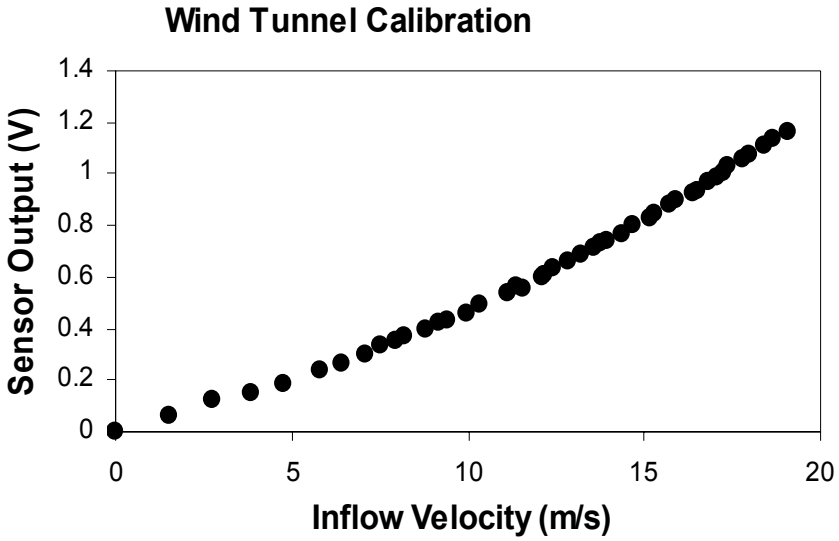

Figure 9: Measured response of the sensor to airflow.

Reduced model of haircell sensors

In order to use the sensor for control, it is important to understand the transfer function of individual sensors to flow field (Figure 10). However, the transfer function between the output and the flow rate input is not linear, but rather parabolic. In order to provide fast control algorithms for MAV maneuvering, the response curve must be simplified into a reduced order model. Belinda Batten's group at the Oregon State University undertook the task of developing reduced order models.

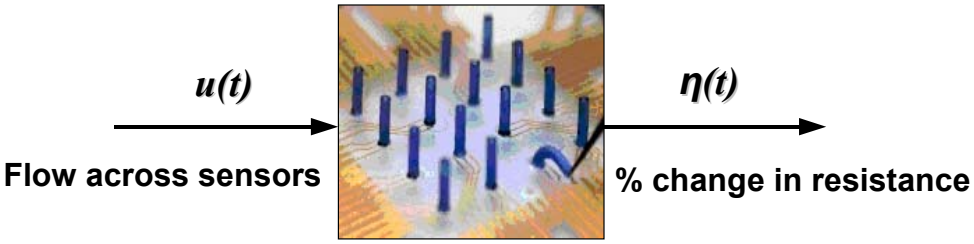

Figure 10: Transfer function of a haircell flow sensor.

Flow field visualization of the vicinity of a hair is plotted in Figure 11, using the reduced order model instead of the differential equation model.

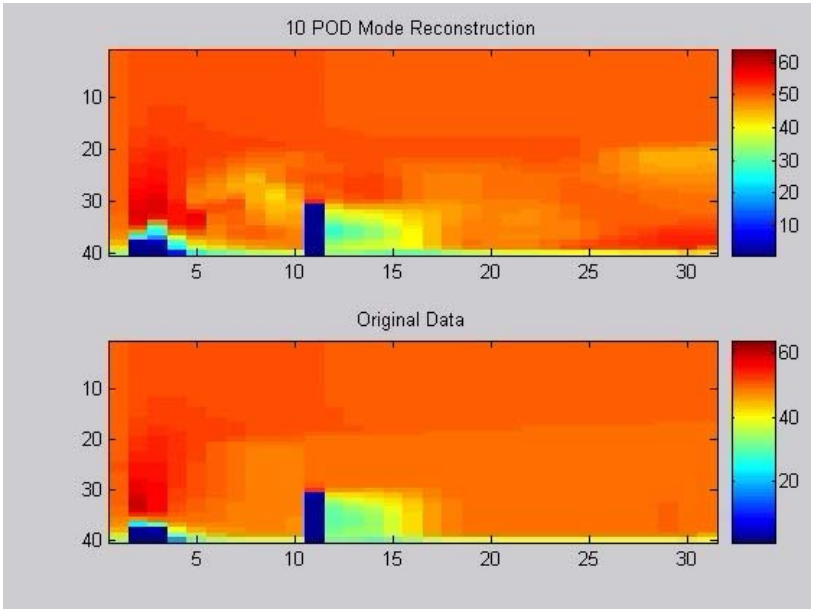

Figure 11: Flow pattern behind a haircell sensor as predicted by a reduced order model.

Flow characteristics studies in wind tunnels

The flow field has been characterized using a particle imaging velocimetry system (PIV). The method involves seeding the flow with light-reflecting particles and using a digital video system to monitor the position of each particle over time (Figure 12). The PIV method therefore provides faithful visual representation of the flow field. We mounted sensors on the airfoils as well to correlate the sensor output to the visualized flow field. Fig. 9 shows the flow field over an airfoil wing. Haircell sensors are embedded in the airfoil themselves.

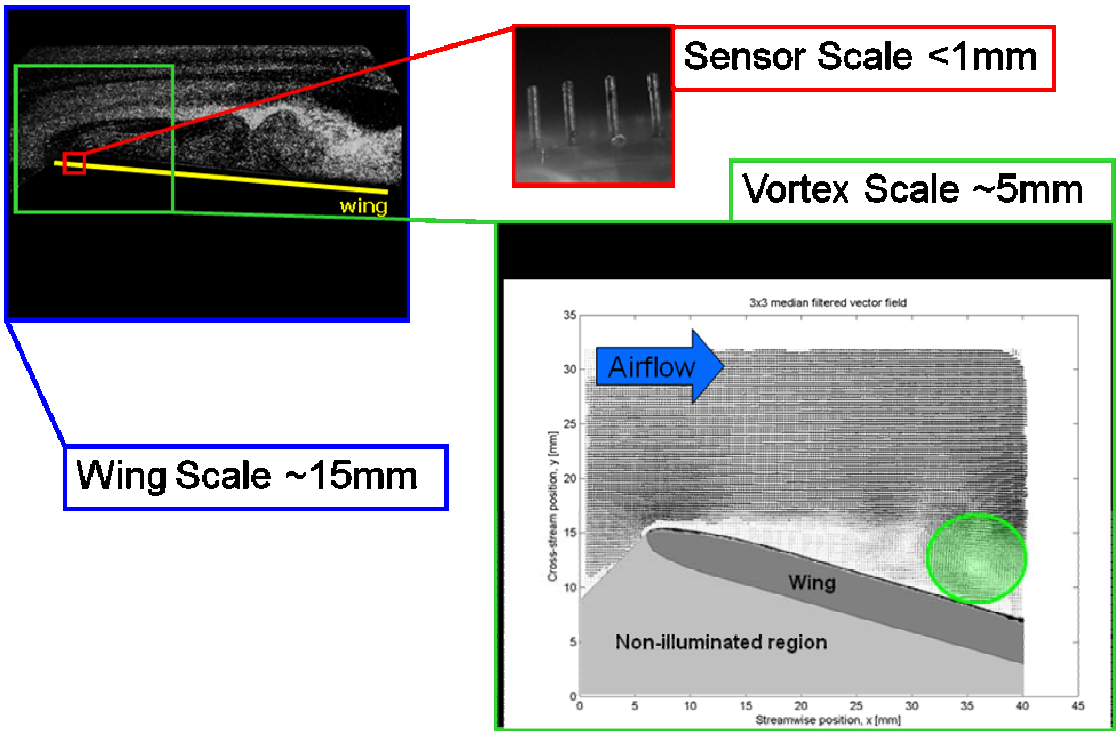

Figure 12: Particle imaging velocimetry (PIV) measurement is used to characterize the flow field. A representative frame is illustrated..

At certain angles of attack, the flow separates from the leading edge of the airfoil and develops into turbulent structures (Figure 13 and Figure 14).

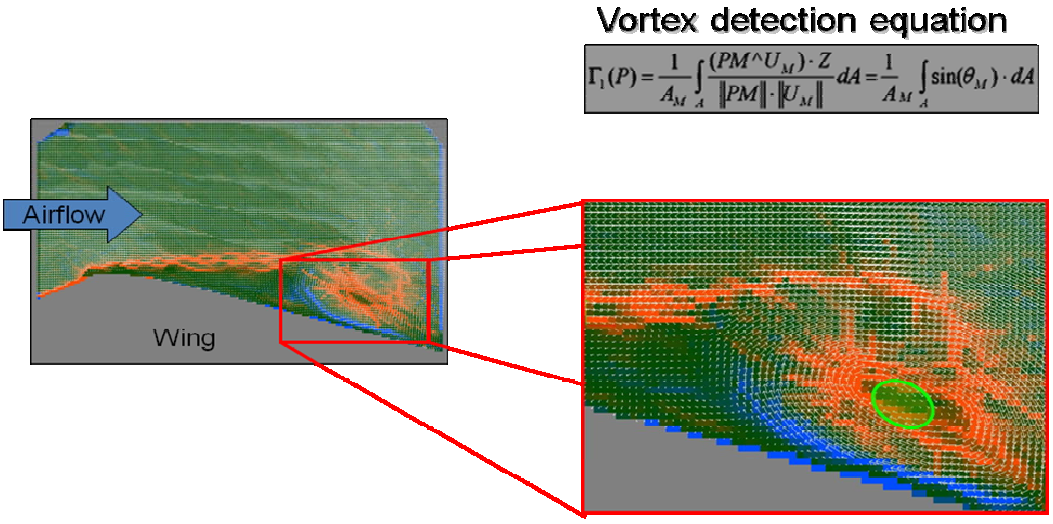

Figure 13: A frame after imaging process to illustrate the presence of vortex and boundary layer separation.

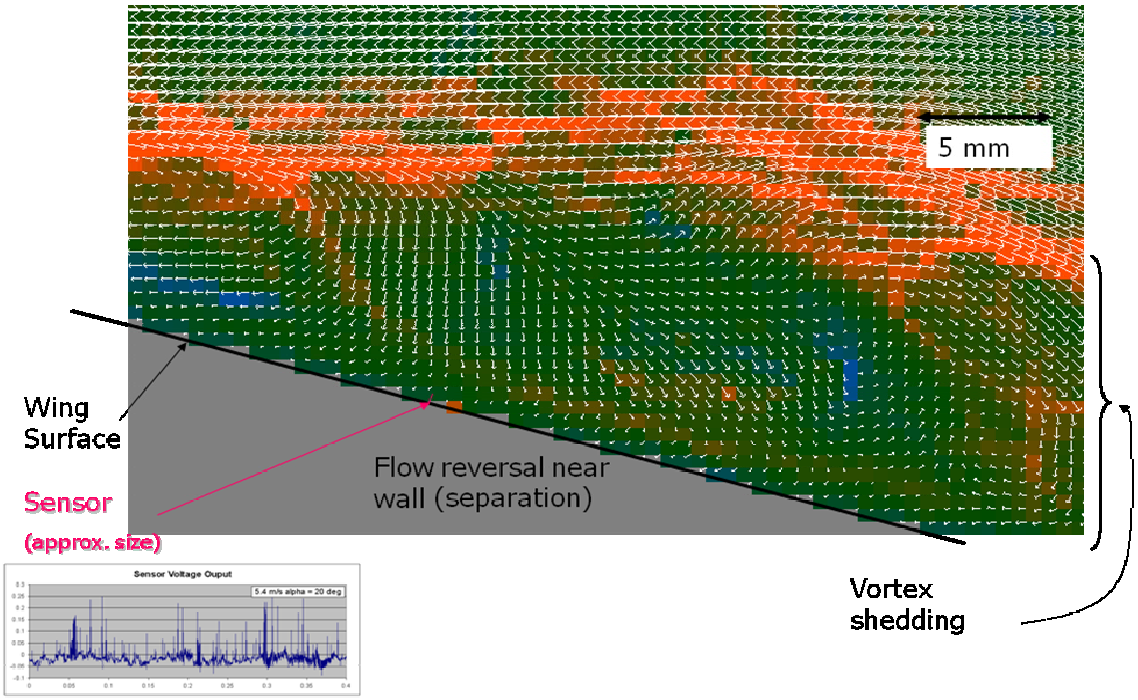

Figure 14: The PIV measurement superimposed with a time-trace of a single haircell located on the wing.

Vortex Detection and Tracking

Data consist of the planar TRPIV results at three chord Reynolds numbers and four angles of attack. Figure 15 illustrates instantaneous velocity vector data at four angles of attack at Re = 14,700 with the x and y coordinates normalized by the chord length, c. Note that (x,y) = (0,0) corresponds with the leading edge coordinate. Also, the field of view is only 25% of the chord length. The darkened region below the wing surface was not illuminated by the laser and contains no velocity data. Individual vector fields are similar for the other Re values. The vector plots clearly identify the separated flow region and the large recirculation or swirl occurrences.

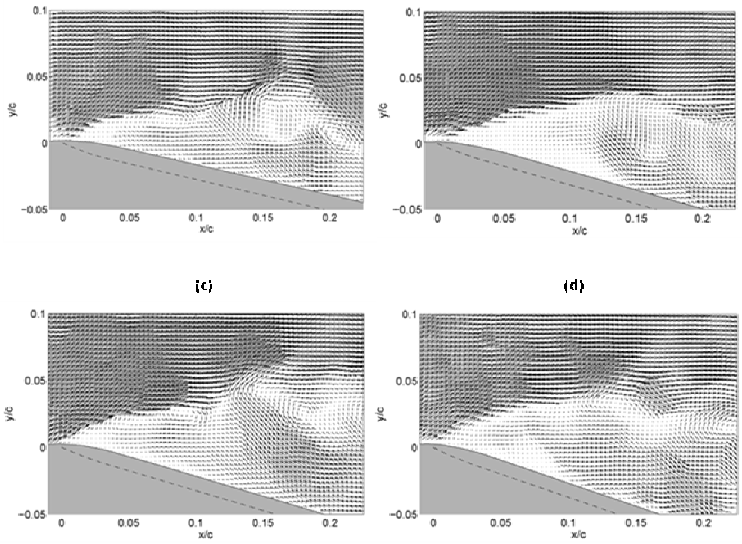

Figure 15: Instantaneous velocity vector fields for Re=14,700 at angle of attack (a) 14° (b) 16° (c) 18° (d) 20°.

Figure 16 illustrates a time resolved sequence of velocity vector fields at one half the sampling rate, or 4 ms time separation, for the case of $\alpha = 14°$ and Re = 14,700. The dots show the vortex location at the four times. Here it can be observed that large vortical structures tend to convect downstream. Since their motion is relatively fast (and dependent on the Re as shown later) the resolution of the convective velocity is limited by the time resolution of the TRPIV, in this case 500 Hz sampling rate.

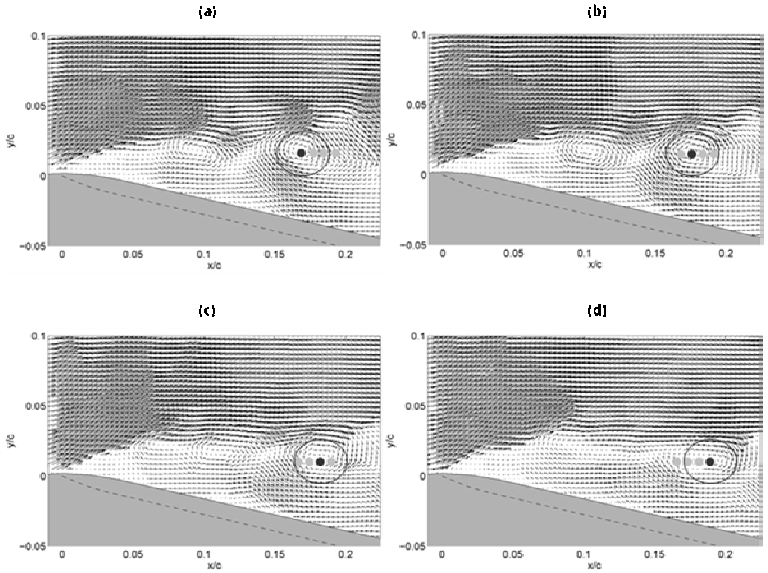

Figure 16: Time sequence of velocity fields, Re=14,700, 14° angle of attack (a) 44, (b) 48, (c) 52, (d) 56 ms. The enclosed region identifies a swirl element as it is convected downstream.

The u and v components of velocity were analyzed for spectral characteristics. Because the data were time resolved a time trace of the velocity components could be examined at a given point in the flow field. Four points were examined that spanned vertically across the separated region at x/c = 0.2 for each Reynolds number and angle of attack. The spectral plots are not shown but no dominant frequency appeared.

Figure 16 shows instantaneous contours of Γ^* at a Reynolds number of 14,700 for all angles of attack. The regions of highest clockwise local swirl ($\Gamma^*<0$) are located in the high shear region away from the wing surface, as separation occurs very near the leading edge. The vortices appear to convect in the shear region which is found to detach further from the wing surface as α increases. That is, the angle of the line of Kelvin-Helmholtz instability beginning at the separation location forms an angle greater than α with the wing surface as α increases. Very near the wing surface there is a series of counterclockwise rotating structures along the surface. The separation region between these two dominant rotating structures does not contain strong swirl components, although the flow is seen to clearly recirculate from the vector plots shown in Figure 15.

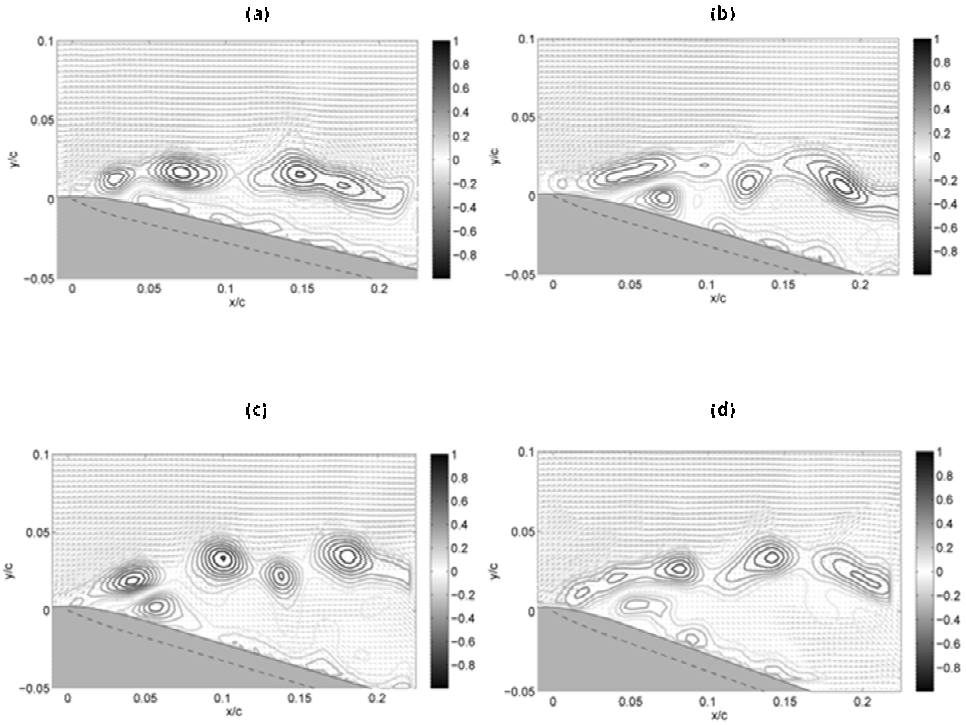

Figure 17: Γ* contours, Re=14,700 at angle of attack (a) 14° (b) 16° (c) 18° (d) 20°.

To show the time evolution of these contours, Figure 18 illustrates a time sequence for the same conditions given in Figure 17.a and the same vector fields given in Figure 16. The structures in the shear layer convect downstream in a systematic manner, while the near wall structures seem not to move. The magnitude of the large swirl elements does not change significantly during convection, at least within the field of view of these data sets.

In the identification of the strongest vortical structures a threshold of$|\Gamma^*| \geq 0.7$ was applied. Based on this the structures near the wall are not detected but rather only the structures in the shear region. It is these clockwise rotating vortices which are the focus of the convective velocity results presented next. The vertical lines in Figure 18 denote the downstream position of the centers of these vortices as defined by the geometric mean position of the $|\Gamma^*| = 0.7$ contour. When those positions are plotted over time the progression can be seen as in Figure 18.e.

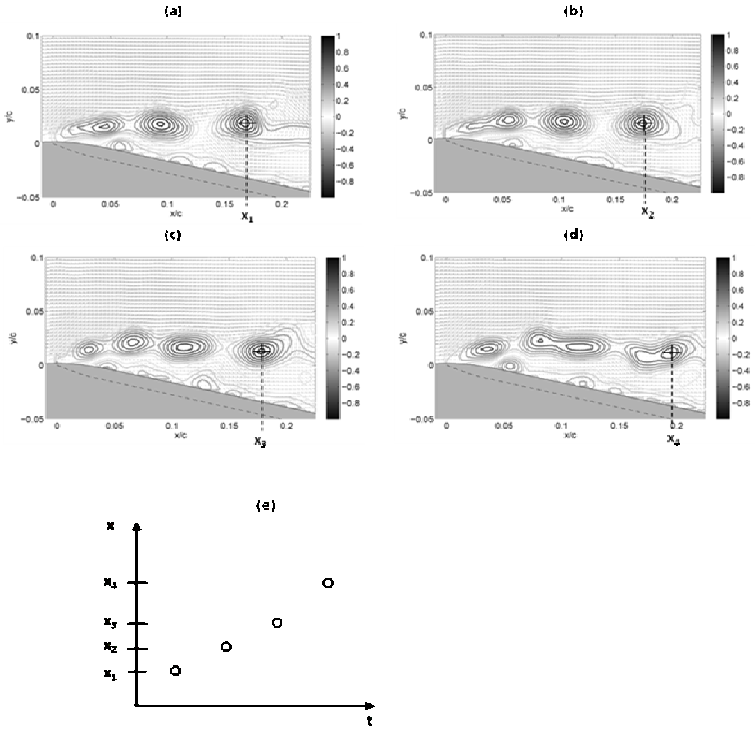

Figure 18: Time sequence of Γ* fields for Re=14,700 and 14° angle of attack (a) 44 ms (b) 48 ms (c) 52 ms (d) 56 ms. Vertical lines indicate the position of recorded vortices. (e) Plot of vortex x positions over time.

The centers of the detected vortices, or swirl regions, were determined at all time steps for each time series, which were two seconds long resulting in 1000 data sets for each flow condition. As an example Figure 19.a illustrates the position versus time for $|\Gamma^*| = 0.7$ contour centers for the first 100 samples of the 20° Re = 14,700, U_∞ = 1.1 m/s case. The distance traveled per sample time was used to calculate the x directional velocity component of these structures. The actual velocity is not necessarily only along the x direction, but this is chosen to determine the downstream convection rate for vortical structures generated at separation. Figure 19.b shows the same results for Re = 66,700, U_∞ = 5.0 m/scase. For this case the convective behavior of the vortices is not as clear due to the scatter of vortex locations. One contributing factor to this scatter is the sampling period which for all cases was held constant at 2.0 ms. For the Re = 14,700 case this represents 1.1% of the convective time scale, τ_c, taken as c/U_∞, whereas for the Re = 66,700 case 2 ms is about 5% of the convective time scale. Filters, discussed below, were employed to reduce the effect of high frequency fluctuations in the flow and allow for more accurate vortex tracking.

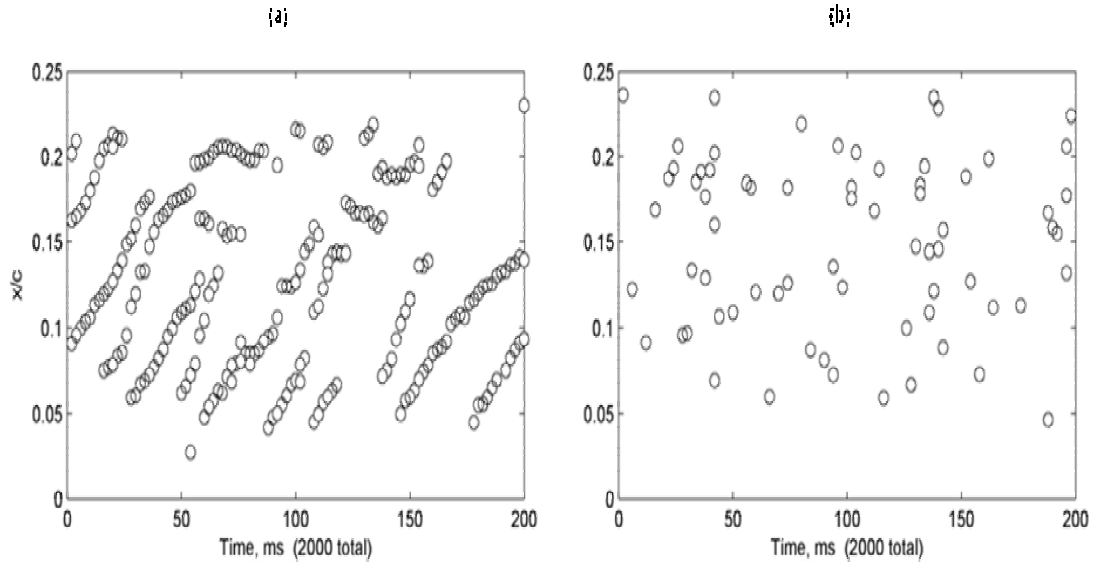

Figure 19: Vortex center positions for (a) Re = 14,700 and (b) Re = 66,700 cases.

The POD filter was applied and Figure 20.a shows the cumulative modal energy content for Re = 14,700. In general, the amount of energy in the lower order modes increases with increasing angle of attack for α=14, 16 and 18°. However for 20° the energy level drops to values between the 14 and 16° cases beyond mode 4. This can be seen most clearly in Figure 20.b, which shows only the first 30 modes. This trend may indicate larger energy content in the modes representative of smaller scale turbulence for the highest angle of attack.

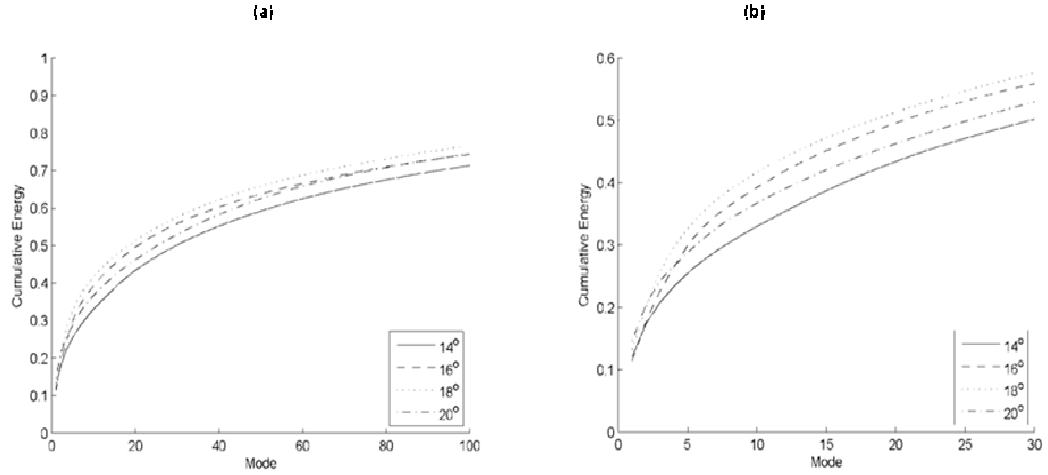

Figure 20: Modal energy plots for all angles of attack for the Re = 14,700 case (a) for the first 100 modes and (b) the first 30 modes.

Spectral analysis

As previously mentioned, no clearly defined frequency was detected from the flow velocity field spectral analysis. Alternatively, the time dependent nature of the detected vortices was studied using the transient characteristics of Γ^*. The strategy for evaluating the transient nature of Γ^* is to look at the temporal autocorrelation of Γ^*, denoted ρ_{Γ^*}, at all spatial locations. A cyclic vortex shedding process at a given point should be correlated at its dominant time period as well as at its harmonics. For example, if a vortex shedding process is observed with a period of 20 ms, then the autocorrelation of Γ^*, should show increased amplitude at 20ms and its harmonic values. The root mean square (RMS) value of ρ_{Γ^*}, denoted here as$\sigma(\rho_{\Gamma^*})$,is used as a measure of the amplitude.A high value of$\sigma(\rho_{\Gamma^*})$ indicates a location where the Γ^* function is highly correlated at specific time intervals, over all time, i.e. resembling a cyclic process.

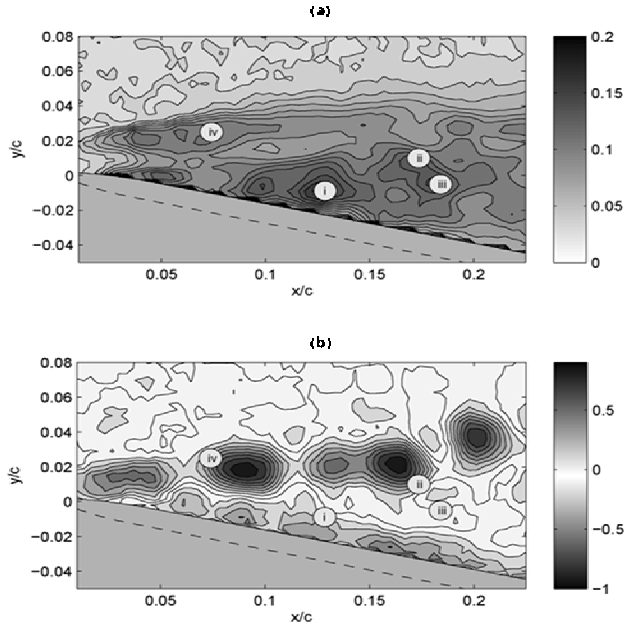

Figure 21: (a) RMS value of the temporal autocorrelation of Γ*, s(rΓ*), at all locations in the field of view for the Re=14,700 and a=14° case. The maximum s(rΓ*) is denoted as point (i), secondary peaks as (ii) and (iii) and the shear layer peak is denoted as (a) are shown to illustrate their location with respect to the shear layer shedding.

Figure 21.a displays $\sigma(\rho_{\Gamma*})$ for the case of 14° angle of attack and Re = 14,700. Four locations are indicated in the figure which represents regions of the largest values of $\sigma(\rho_{\Gamma*})$. These are numbered in decreasing order of magnitude.The three largest values are within the recirculation zone of separation. The fourth is in the shear layer near the leading edge. To put this in perspective, Figure 21.b plots a single time frame of Γ^*. The maximum$\sigma(\rho_{\Gamma*})$ valuesare located in the recirculating separation region significantly below the shear layer, while the fourth point lies along the shear layer at y/c ~0.02.

Based on these results it was decided to further examine the POD filtered results to help determine the nature of the cyclic process. The modes were determined after removing the mean flow which is denoted mode 0.Frequency spectra of the mode amplitude time series, $a_k(t)$, were also found. Figure 22.a plots the vector map, $d_1(x,y)$ for mode 1 along withcontours of $\Gamma^*$for the mode 1 vector field. Since a mode describes the variance of the flow field the mode map in the area of the constant freestreamwill be near zero. Mode 1 displays a largeupwash of velocity in the separated region. This can be considered an upwash or downwash at any given moment depending on the instantaneous sign of the amplitude time series, $a_1(t)$. This feature appears to be part of a larger flow structure further downstream from the x/c = 0.25 boundary of the field of view. This large pattern does not result in a significant value of Γ^* due to its large scale. The contours of Γ^*associated with the shear layer for mode 1 are weak with values of $|\Gamma^*|< 0.2$ and are not indicative of swirl but rather the velocity gradient in the region of the shear layer. The frequency response of $a_1(t)$ is given in Figure 22.b. The primary spatial structure observed in Figure 22.a is larger than most of the vortices observed in the flow and has a frequency response in the range of 1-3 Hz, with no high frequency component.

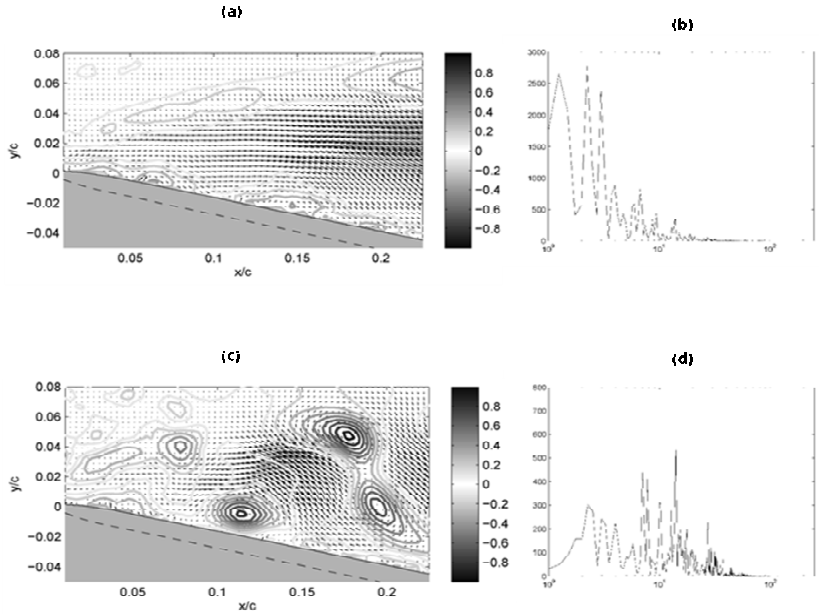

Figure 22: POD for Re = 14,700, 14° angle of attack; (a) mode 1 vector field, $d_1(x,y)$ with Γ^* contours and (b) frequency spectrum of the amplitude time series, $a_1(t)$, (c) mode 2 vector field, $d_2(x,y)$ with G^* contours and (d) frequency spectrum of the amplitude time series, $a_2(t)$, (e) mode 3 vector field, $d_3(x,y)$ with G^* contours and (f) frequency spectrum of the amplitude time series, $a_3(t)$, (g) mode 4vector field, $d_4(x,y)$ with G^* contours and (h) frequency spectrum of the amplitude-time series,$a_4(t)$

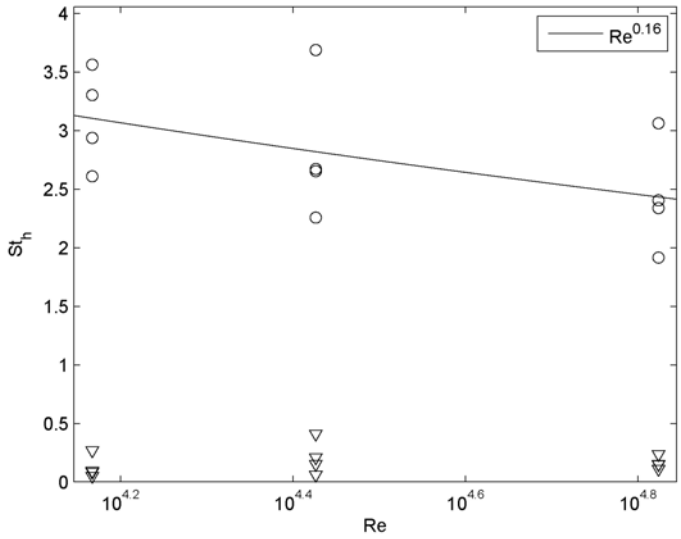

Figure 23: Strouhal numbers for the max shear region frequencies of Γ*. The separated region frequencies denoted by triangles and the shear region frequencies are indicated by circles.

All 11 cases were investigated using the POD analysis to determine dominant frequencies. Two dominant frequency signals of Γ^* were obtained for each case, one in the separated region and one in the shear layer. To quantify these, the maximum $\sigma(\rho_{\Gamma*})$ was located and the dominant frequency at that location was determined. The location for evaluation in the shear region was chosen as x/c = 0.075 and y/c = 0.035 which is close to location (iv) shown in Figure 23. A highpass filter was used to separate the high frequency signal in the shear region from the low frequency signal. The higher frequency cut-off was two times the low frequency signal value determined in the recirculating region. The frequency, f, was nondimensionalized as a Strouhal number, $St = fh/U_\infty$, where $h = c\sin(\alpha)$ is the projected height of the wing, and U_∞ is the freestream velocity. Results are plotted in Figure 23 versus Re. The various values at each Re are the results for different angles of attack. The frequencies observed in the separated region are shown as triangles and are seen to have an averageStrouhal number of 0.164.This matches with observations by Abernathy [9] and Roshko [10] of shedding frequencies of bluff bodies. Overall, a slight increase of St with increasing α was observed although this was not exclusively the case at each Reynolds number.

An average shear region Strouhal number was determined by averaging over all angles of attack for each Reynolds number and then a linear fit was applied and is shown as the dashed line in Figure 23. The averagedStrouhal number in the shear region is seen to decrease slightly with increasing Reynolds number as $Re^{-0.16}$. Further study is needed to better understand the scatter in these data with α and to determine if the trend of decreasing St with increasing Re is observed over larger data sets.

Personnel supported:

Chang Liu, Associate Professor of Electrical and Computer Engineering, University of Illinois at Urbana-Champaign.

Jonathan Engel, graduate student. Graduated with a Ph.D. and now works at Honeywell Corporation.

Nannan Chen, graduate student pursuing Ph.D. degree at the University of Illinois.

James A. Liburdy, *J.R. Welty Professor* of Mechanical engineering, Oregon State University

Daniel R. Morse, PhD Graduate Student, Oregon State University

Belinda Batten, Chair, Mechanical Engineering, Oregon State University

John R. Singler, postdoctoral researcher, Mechanical Engineering Department, OSU

Ben Dickinson, Graduate student, Mechanical Engineering Department, OSU

Publications:

Morse, D.R. and Liburdy, J.A., 2008, "Vortex Dynamics and Bi-Modal Shedding of a Flat Airfoil at Low Reynolds Numbers and High Attack Angles", J. Fluids Engineering, in final revision.

Chen, N., et al., *Design and Characterization of Artificial Haircell Sensor for Flow Sensing With Ultrahigh Velocity and Angular Sensitivity.* IEEE/ASME Journal of Microelectromechanical Systems (JMEMS), 2007. **16**(5): p. 999-1014

Interactions/Transitions

a. participation and presentations at meetings

Chen, G., Lin, Z., Morse, D.R., Snider, S., Apte, S., Liburdy, J.A., Zhang, E., "Multiscale Feature Detection in Unsteady Separated Flow", Int. J. Num. Analysis and Modeling, In Print, 2008

Morse, D.R. and Liburdy, J.A., 2008, "Experimental Time-Resolved Flow Features of Separation Over an Elliptic Leading Edge" Proc. 46th AIAA Aerospace Sciences Meeting and Exhibit, Reno NV.

Chen, G., Morse, D., Snider, S., Apte, S., Liburdy, J. and Zhang, E., 2008, "Detection and Analysis of Separated Flow Induced Vortical Structures", Proc. 46th AIAA Aerospace Sciences Meeting and Exhibit, Reno NV.

Morse, D.R and Liburdy, J.A. 2007, "Vortex Detection and Characterization in Low Reynolds Number Separation", Proc. ASME IMECE 2007-43011, Seattle, WA, USA

Morse, D.R and Liburdy, J.A., 2007, "Dynamic Characteristics of Flow Separation from a Low Reynolds Number Airfoil", Proc. ASME FEDSM-37803, San Diego, CA.

Chen, G., Morse, D., Snider, S., Apte, S., Liburdy, J. and Zhang, E., 2007, "Multiscale Filtering and Detection of Separated Flow Induced Vortical Structures", NSF Workshop on Multiscale Theory and Modeling, June, 2007.

Morse, D.R. and Liburdy, J.A., 2007, "Feature Detection for Time Resolved Velocity Data for Flow Separation Over an elliptic Leading Edge" American Physical Society, Fluid Dynamics Division Meeting, Salt Lake City, UT.

Chen, J., et al. *Artificial Lateral Line and Hydrodynamic Object Tracking*. in *MEMS 2006 Conference*. 2006. Istanbul, Turkey

Engel, J., et al. *Development and Characterization of an Artificial Hair Cell Based on Polyurethane Elastomer and Force Sensitive Resistors*. in *The 4th IEEE International Conference on Sensors*. 2005. Irvine, California.

Engel, J., et al. *Multi-Layer Embedment of Conductive and Non-Conductive PDMS for All-Elastomer MEMS*. in *The 12th Solid State Sensors, Actuator, and Microsystems Workshop (Hilton Head 2006)*. 2006. Hilton Head Island, SC

Engel, J., et al. *Multi-Walled Carbon Nanotube Filled Conductive Elastomers: Materials and Application to Micro Transducers*. in *MEMS 2006 Conference*. 2006. Istanbul, Turkey

Liu, C., et al. *Polymer Micro and Nano Scale Fabrication Technology Development for Bioinspired Sensing*. in *IEEE International Conference on Nano/Micro Engineered and Molecular Systems*. 2006. Zhuhai, China

b. consultative and advisory functions **None**
c. transitions

Transition efforts are being made to Boeing and Baxter. Boeing is interested using the sensor for monitoring flow on large aircraft wings. Baxter is interested in using the sensor for monitoring flow in medical assisted-living instruments.

New Discoveries, inventions and patent disclosure

None.

Honors/Awards

James A. Liburdy, promoted to *J.R. Welty Professor* of Mechanical engineering, Oregon State University.

Chang Liu, elected a member of the Center for Advanced Studies of the University of Illinois.

References:

1. McCullough, G.B. and D.E. Gault, *Examples of three representative types of airfoil-section stall at low speeds*. 1951, NACA tech Note 2502.
2. Carmichael, B.H., *Low Reynolds number airfoil survey, Volume 1*. 1981, NASA Contractor report: Capistrano Beach, CA 92624.
3. Mueller, T.J. and J.D. DeLaurier, *Aerodynamics of small vehicles.* Annu. Rev. Fluid Mech., 2003. **35**: p. 89-111.
4. Bishop, R.E.D. and A.Y. Hassan, *The lift and drag forces on a circular cylinder in a flowing fluid.* Proc. Roy. Soc. London Ser. A, 1964. **277**: p. 32-50.
5. Berger, E. and R. Wille, *Periodic flow phenomena.* Annu rev fluid mech, 1972. **11**: p. 313-40.
6. Mair, W.A. and D.J. Maull, *Bluff bodies and vortex shedding - a report on euromech 17.* Journal of Fluid Mechanics, 1971. **45**(2): p. 209-224.
7. Chen, N., et al., *Design and Characterization of Artificial Haircell Sensor for Flow Sensing With Ultrahigh Velocity and Angular Sensitivity.* IEEE/ASME Journal of Microelectromechanical Systems (JMEMS), 2007. **16**(5): p. 999-1014.
8. Hinze, J.O., *Turbulence*. 1959, New York: McGraw-Hill.
9. Abernathy, F.H., *Flow over an inclined plate.* J. Basic Eng., 1962. **84**: p. 380-388.

10. Roshko, A., *On the drag and shedding frequency of two dimensional bluff bodies*. 1954, NACA Technical note 3169.